Nano Research 2016, 9(9): 2772–2781
DOI 10.1007/s12274-016-1166-y
Research Article
ISSN 1998-0124
CN 11-5974/O4

Unraveling the correlation between the remanence ratio and the dipolar field in magnetic nanoparticles by tuning concentration, moment, and anisotropy

Bingqian Geng, Zongling Ding, and Yongqing Ma (✉)

Anhui Key Laboratory of Information Materials and Devices, School of Physics and Materials Science, Anhui University, Hefei 230601, China

Received: 30 January 2016
Revised: 16 May 2016
Accepted: 2 June 2016

© Tsinghua University Press and Springer-Verlag Berlin Heidelberg 2016

KEYWORDS
magnetic nanoparticle,
cobalt ferrite,
dipolar interaction,
remanence ratio

ABSTRACT

Well-dispersed, uniform cobalt ferrite ($CoFe_2O_4$) nanoparticles (NPs) with diameters of 9, 11, 14, and 30 nm were synthesized by thermal decomposition of a metal–organic salt. Multiple variables, including the interparticle distance, moment, and anisotropy, were altered by dilution in a silica matrix and reduction in hydrogen to reveal the intrinsic correlation between the ratio of remanence to saturation magnetization (M_r/M_s) and interparticle dipolar interactions, the strength of which was estimated by the maximum dipolar field H_{dip}. To date, this correlation has not been systematically investigated experimentally. To prevent the particles from agglomerating, the reduction was performed after dilution. The results revealed that the correlation between M_r/M_s and H_{dip} roughly followed $M_r/M_s \propto 1/\lg H_{dip}$ independent of the size, distance, moment, and anisotropy of the magnetic nanoparticles. In particular, the correlation was closer for the nanoparticle systems that had higher concentrations or moments, that is, stronger dipolar interactions. For the single-phase $CoFe_2O_4$ nanoparticles, deviation from $M_r/M_s \propto 1/\lg H_{dip}$ can be attributed to the effects of surface spin, and for the slightly reduced nanoparticles, this deviation can be attributed to the pinning effect of $CoFe_2O_4$ on $CoFe_2$.

1 Introduction

Nanoparticles (NPs) composed of ferro- or ferrimagnetic materials, such as metals, alloys, and spinel ferrites, have been extensively investigated because of their unique magnetic properties [1–3], which can vary from those of their bulk counterparts, and because of their broad range of applications [4, 5].

The practical application of NPs requires suitable particle size and concentration. NPs with 5–100 nm diameters have sizes comparable to those of biological components such as proteins (5–50 nm) and viruses (20–200 nm) [6]. Surface modification or functionalization of NPs with non-magnetic materials,

Address correspondence to yqma@ahu.edu.cn

such as upconversion luminescent materials [7], SiO_2 [8], quantum dots [9], or a solvent layer [10], has greatly expanded their applications in the fields of cell therapy research, cancer diagnosis and monitoring, and ferrofluids [10]. Inevitably, modification or functionalization (i.e., dilution in the non-magnetic matrix) changes the concentration of NPs, which plays a crucial role in their practical application. Simply exemplified by magnetic fluids (ferrofluids, ferrocolloids) with a particle size of approximately 10 nm (single domain), magnetic NPs participate in Brownian motion at low concentrations. In contrast, at high concentrations, NPs interact with each other to form aggregates, greatly influencing the diffusional and hydrodynamic properties of ferrofluids [10].

Fundamentally, the effects of particle size and concentration on the magnetic properties of NPs can be attributed to two types of energies: anisotropy and interparticle dipolar interaction (IPDI). Below a certain size (generally, 10–20 nm), NPs can exhibit a unique form of magnetism called superparamagnetism [11] with zero theoretical coercivity (H_c) and remanence (M_r); In addition, in the case of small particles, the interactions between the surface spins of different particles affect the surface anisotropy, increasing the effective anisotropy [12]. It has been reported that the surface anisotropy constants of thin films and NPs are many orders of magnitude higher than that of the bulk material [13]. The concentration of NPs directly reflects the strength of the IPDI, which can be expressed by the maximum dipolar field H_{dip}, defined as

$$H_{dip} = 2\mu/d^3 \quad (1)$$

where μ is the particle moment ($\mu = M_s \times V_m$; M_s is the saturation magnetization, and V_m is the magnetic grain volume), and d is the distance between particles (center to center), which is inversely proportional to the NP concentration. Based on the strength of the IPDI, the NPs spontaneously form various architectures of one-dimensional chains, hexagonal-close-packed two-dimensional arrays, and three-dimensional clustered aggregates, as shown in a transmission electron microscopy (TEM) analysis [11], which consequentially affect the magnetic properties of the NPs. Indeed, the effects of the IPDI are quite complex, and some inconsistent results have been reported [14, 15].

To date, the effects of the IPDI on the magnetic properties of NPs have not been investigated experimentally, and the key issue lies in the design and preparation of the NP system. For example, the Stoner–Wohlfarth model [16] indicated that the remanence (M_r) to saturation magnetization (M_s) ratio M_r/M_s is 0.5 for uniaxial anisotropy, and this value is 0.832 ($K_1 > 0$) or 0.87 ($K_1 < 0$) for cubic anisotropy in the case of non-interacting single-domain particles with a randomly oriented easy axis [17]. However, many authors have reported values of M_r/M_s smaller than the theoretical value for cubic cobalt ferrites ($CoFe_2O_4$) [18–22] and for composites of hard $CoFe_2O_4$ and soft Co–Fe alloy [23–25]; this discrepancy has recently been attributed to the effects of particle size and crystallinity. Examination of the scanning electron microscopy (SEM) and TEM results for these materials revealed that the NPs were heavily agglomerated. In such agglomerated systems, at least the IPDI should be considered; in addition, the broad size distribution, effective anisotropy, and exchange–coupling interactions synergistically affect the magnetic properties of the NPs. Clearly, to thoroughly investigate the effects of the IPDI on the magnetic properties of NPs, it is important to first synthesize high-quality magnetic NPs with uniform size and high dispersity to exclude the size distribution effects and the exchange–coupling interaction, that is, to obtain pure dipolar interactions.

Recently, using a DC magnetron sputtering method combined with a high-resolution electron beam lithography technique, perpendicular three-island Co/Pd magnetic clusters were deposited on a Si substrate. The effects of dipole–dipole interactions among magnetic clusters on their switching field were investigated. By optimizing island size, thickness, gap, anisotropy, and saturation magnetization, a three-island cluster with six stable flux states was realized, which has potential applications in flexi-programmable logic devices [26]. In the present work, we used the thermal decomposition of a metal–organic salt to prepare well-dispersed, uniform $CoFe_2O_4$ NPs in four sizes (9, 11, 14, and 30 nm). The concentration, moment, and anisotropy of the $CoFe_2O_4$ NPs were altered by dilution in a SiO_2 matrix and/or by reduction in H_2

atmosphere to systematically reveal the intrinsic correlation between H_{dip} and M_r/M_s.

2 Experimental

2.1 Preparation of $CoFe_2O_4$ NPs

In a 1,000-mL three-necked round-bottom flask, iron acetylacetonate (9.586 g), cobalt acetylacetonate (3.526 g), oleic acid (80 mL), oleylamine (80 mL), and benzyl ether (400 mL) were mixed by magnetic stirring under a flow of nitrogen (99.999%). The mixture was heated at 120 ℃ for 0.5 h to remove air and moisture, at 200 ℃ under reflux for 2 h, and then at 290 ℃ for 1 h. After the mixture was cooled naturally to room temperature, absolute ethanol (approximately 500 mL) was added to produce a precipitate. The precipitate was separated via centrifugation and then washed with absolute ethanol several times to obtain $CoFe_2O_4$ NPs. The particle size was varied by altering the intermediate treatment temperature.

2.2 Dilution of $CoFe_2O_4$ NPs in a SiO_2 matrix

$CoFe_2O_4$ NPs were added to a solution of cyclohexane (400 mL), polyethylene glycol (25 mL), tetraethyl orthosilicate, and ammonia, and then stirred mechanically for 24 h. Ethanol was added to form a precipitate. The precipitate was isolated by centrifugation and then washed with ethanol and water to remove unreacted molecules. The precipitate was dried at 80 ℃ for 6 h to obtain diluted $CoFe_2O_4$ NPs.

2.3 Reduction of $CoFe_2O_4$ NPs

The reduction reactions were performed in a H_2-containing atmosphere (500 sccm, 96% N_2 + 4% H_2) to yield a composite of $CoFe_2O_4$ and $CoFe_2$ alloy. The diluted 14-nm $CoFe_2O_4$ NPs were reduced at 300 and 400 ℃ for 4 h. The undiluted 30-nm $CoFe_2O_4$ NPs were reduced at 300 ℃ for 4 and 8 h.

2.4 Characterization

Crystal structures were determined by X-ray diffraction (XRD) with an X-ray diffractometer (DX-2000 SSC, Dandong Fangyuan Instrument Company, Dandong, Liaoning, China) with Cu Kα irradiation (λ = 1.5406 Å) in the scanning range of 20°–80° and with a step size of 0.02°. High-resolution transmission electron microscopy (HRTEM; JEOL JEM-2100, Tokyo, Japan) was used to observe the particle size and morphology. The magnetic properties of the NPs were investigated using a superconducting quantum interference device physical property measurement system (PPMS) system (SQUID, PPMS EC-II, Quantum Design Inc., San Diego, CA, USA).

3 Results and discussion

Some of the 9-, 11-, and 14-nm $CoFe_2O_4$ NPs were diluted in a SiO_2 matrix to change the interparticle distance; diluted and undiluted NPs are hereafter referred to as D(9) and UD(9) (9-nm NPs), D(11) and UD(11) (11-nm NPs), and D(14) and UD(14) (14-nm NPs), respectively. To vary the moment and the anisotropy of the NPs, the D(14) NPs were reduced in H_2 at 300 and 400 ℃ to yield composites of $CoFe_2O_4$ and $CoFe_2$ alloy through the following reduction reaction: $CoFe_2O_4 + 4H_2 \rightarrow CoFe_2 + 4H_2O$ [25]. The obtained samples were denoted DR300(14) and DR400(14). As a reference, the undiluted 30-nm $CoFe_2O_4$ NPs were also reduced at 300 ℃ for 4 and 8 h; these are hereafter referred to as UDR4h(30) and UDR8h(30).

CoFe alloy is a typical soft ferromagnet with a maximum M_s of 230 emu·g^{-1} [27] and low anisotropy compared with that of $CoFe_2O_4$; therefore, reduction of the NPs under different conditions changes their moment and their anisotropy. In the composites of soft $CoFe_2$ and hard $CoFe_2O_4$, the effective anisotropy constant K_{eff} was expressed as

$$K_{eff} = f_s K_s + f_h K_h \quad (2)$$

where f_s and f_h are the volume fractions, and K_s and K_h ($K_h > K_s$) are the anisotropy constants of soft and hard phases, respectively [28]. The K_{eff} value of a sample decreases when $CoFe_2O_4$ is reduced to $CoFe_2$.

In previous studies, the reduction was directly performed on undiluted $CoFe_2O_4$ NPs, resulting in severe agglomeration, as shown in Scheme 1(a), because the magnetic NPs were in close contact. The NPs consequently formed aggregates with different sizes and shapes, which affected the magnetic properties.

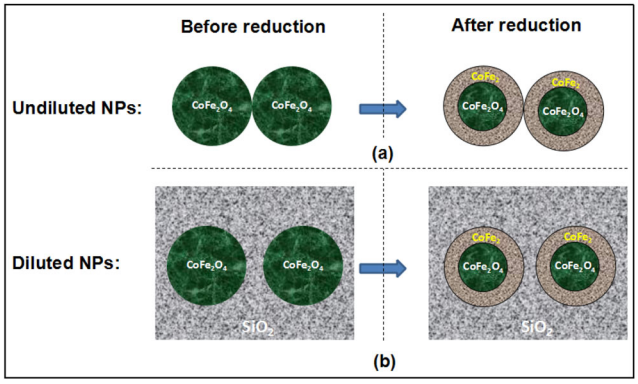

Scheme 1 Schematic plots for the preparation of $CoFe_2O_4$/$CoFe_2$ composites before (left) and after (right) reduction of $CoFe_2O_4$ for the undiluted (a) and diluted NPs in the SiO_2 matrix (b).

Conversely, in the case of the diluted $CoFe_2O_4$ NPs, the SiO_2 matrix prevented the magnetic NPs from aggregating during reduction, as shown in Scheme 1(b).

The TEM images and size histograms in Fig. 1 show that the NPs were approximately 9, 11, 14, and 30 nm; most of the 9-, 11-, and 14-nm particles exhibited a spherical-like morphology, whereas the 30-nm particles presented hexagonal and cubic morphologies. The size distribution range was approximately 2 nm for the 9-nm NPs, 4 nm for the 11-nm NPs, and 8 nm for both the 14- and 30-nm NPs, similar to the value of 26 ± 4 nm for the $CoFe_2O_4$ NPs synthesized by Mazz et al. [29]. In addition, the NPs showed better dispersion and a narrower size distribution than those synthesized by a sol–gel autocombustion method (particle size, 20 ± 7 nm) [19] and a co-precipitation route (particle size, 15–48 nm) [20]. Most of the 9- and 11-nm NPs aligned hexagonally to form two-dimensional arrays as a result of their weak IPDI. However, the 14- and 30-nm NPs formed cluster-like aggregates except for some hexagonal-close-packed arrays, implying that they possessed stronger IPDI than the 9- and 11-nm NPs. This finding is logical because the larger the particle size, the larger the particle moment, which leads to stronger IPDI.

XRD measurements were performed on all samples, and some representative measurements are shown in Fig. 2. Compared with the standard powder diffraction file (PDF) (No. 22-1086) of $CoFe_2O_4$ in Fig. 2(a), the 9-, 11-, 14-, and 30-nm NPs were single phase and crystallized with spinel-type structure, as shown in Figs. 2(b)–2(e). For the reduced samples DR400(14)

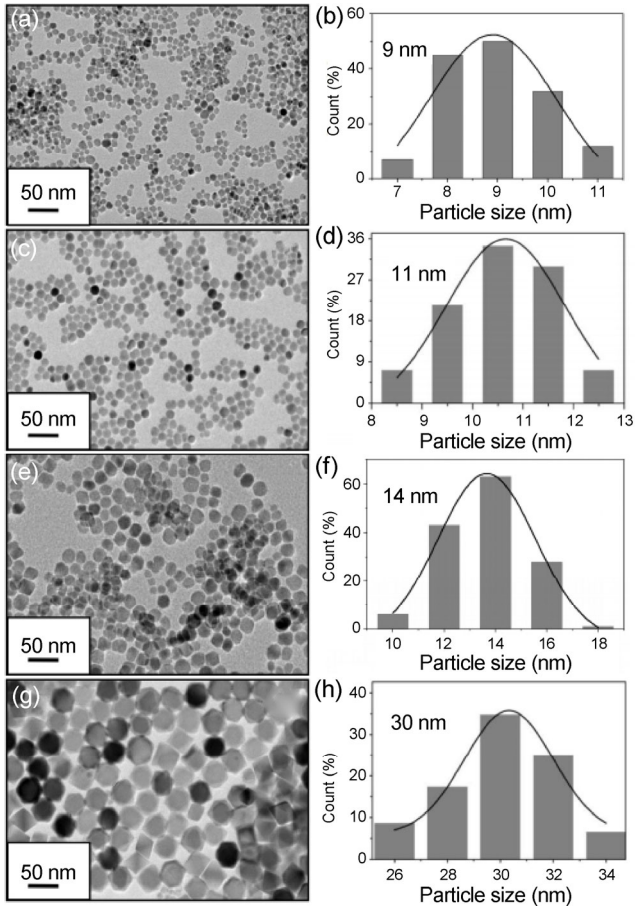

Figure 1 TEM images and size distribution histograms with Gaussian-fitting curve (solid line) for 9-nm ((a) and (b)), 11-nm ((c) and (d)), 14-nm ((e) and (f)), and 30-nm ((g) and (h)) as-prepared $CoFe_2O_4$ nanoparticles.

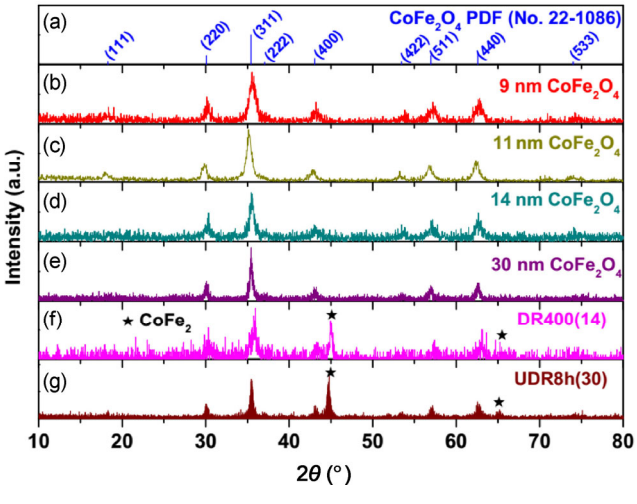

Figure 2 PDF card of $CoFe_2O_4$ (No. 22-1086) (a) and XRD patterns of samples UD(9) (b), UD(11) (c), UD(14) (d), UD(30) (e), DR400(14) (f), and UDR8h(30) (g).

and UDR8h(30), in addition to the diffraction peaks from $CoFe_2O_4$, two extra peaks at 2θ = 44.76° and 65.16° belong to the reflection of (110) and (200) planes from the $CoFe_2$ phase. To observe the microstructural features of the magnetic NPs with and without reduction, HRTEM was performed on undiluted 14-nm particles because the lattice fringes of diluted NPs are difficult to observe owing to the existence of SiO_2 surrounding the magnetic NPs. Figure 3 shows the HRTEM images of undiluted 14-nm NPs that had not been reduced (a) and of UDR4h(30) (b). The fringes with distances of 0.25 nm in Fig. 3(a) and 0.48 nm in Fig. 3(b) correspond to the (311) and (111) crystallographic planes in $CoFe_2O_4$. For UDR4h(30), the fringes with a short distance of 0.28 nm can be observed at the surface of the $CoFe_2O_4$ particles and are attributable to the (100) crystallographic planes in $CoFe_2$.

The dependence of the magnetization (M) of the samples on the applied magnetic field (H), that is, $M(H)$ loops (−7 T < H < 7 T), was measured at temperatures of 10, 50, 100, 150, 200, 250, 300, and 390 K to obtain the coercivity (H_c), M_s, and M_r/M_s values at each temperature. Figures 4 and 5 show representative $M(H)$ loops recorded at 10 and 390 K for the unreduced, diluted and undiluted 9-, 11-, and 14-nm NPs and for the reduced 14- and 30-nm NPs.

The square-root temperature dependence of H_c can be fitted to Kneller's law in the temperature range of 10–390 K [30]; that is

$$H_c = H_{c0}[1 - (T/T_B)^{1/2}] \quad (3)$$

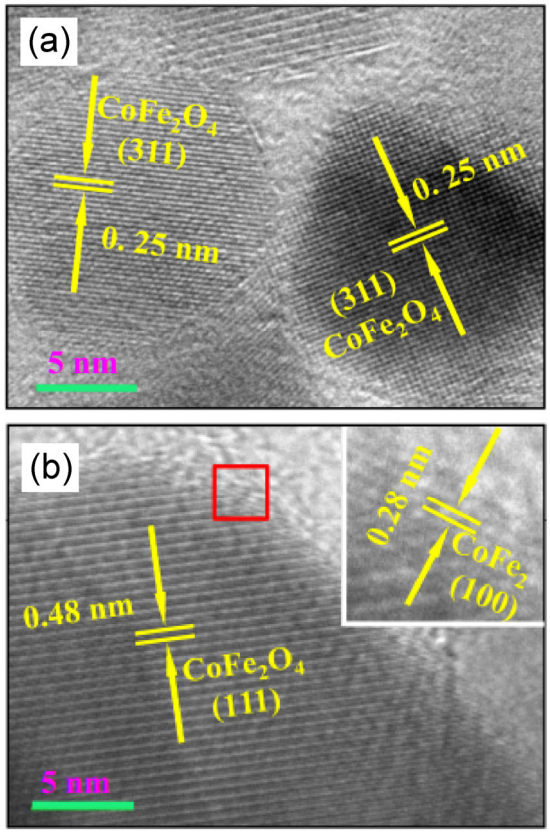

Figure 3 HRTEM images of unreduced 14-nm NPs (a) and of UDR4h(30) (b).

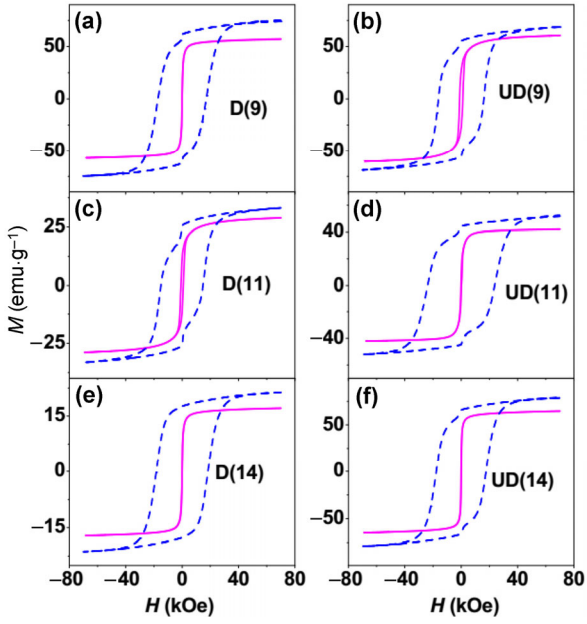

Figure 4 $M(H)$ loops (−7 T < H < 7 T) of the unreduced, diluted and undiluted 9-, 11-, and 14-nm NPs measured at 10 K (dashed) and 390 K (solid).

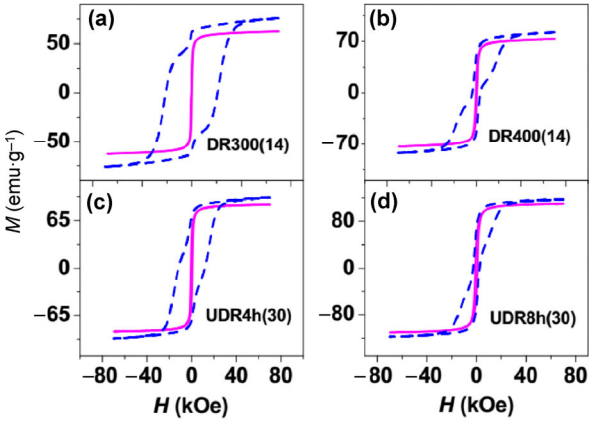

Figure 5 $M(H)$ loops (−7 T < H < 7 T) of DR300(14) (a), DR400(14) (b), UDR4h(30) (c), and UDR8h(30) (d) measured at 10 K (dashed) and 390 K (solid).

where H_{c0} is the value of H_c at 0 K, and T_B denotes the blocking temperature. The UD(11) sample possessed the largest H_{c0} (29.6 kOe) because its particle size was close to the critical size of a single domain [10].

For non-interacting and randomly oriented spherical particles with cubic anisotropy, H_c is given by

$$H_c = 0.64K/M_s \quad (4)$$

where K is the anisotropy constant [12]. The highest value of K at 10 K approaches ~10^7 erg·cm^{-3} for all NPs, which is greater than the value of 1.8 × 10^6–3.0 × 10^6 erg·cm^{-3} reported for bulk $CoFe_2O_4$ because of the interactions between the surface spins of different particles [12].

Based on the given T_B and K, the volume of magnetic grain, V_m, can be calculated according to

$$25k_BT_B = KV_m \quad (5)$$

where k_B is the Boltzmann constant [31]. Therefore, the diameter (D_m) of a magnetic grain for all samples can be obtained, as shown in Figs. 6 and 7. In the case of the 9-, 11-, and 14-nm particles, as shown in Fig. 6 and Fig. 7(a), D_m is smaller than D_{TEM} below a certain temperature, indicating the existence of a canted surface spin layer surrounding the magnetic particles [32]; thus, the moment of a nanoparticle is composed of disordered spins at the particle surface and ordered spins from the particle core with the diameter of D_m, which is known as the core–shell magnetization model. Above this temperature, D_m becomes larger than D_{TEM}, the reasons for which are as follows: First, the surface spins become able to thermally fluctuate, so they can be polarized by the core moments; that is, the surface spins align in parallel with the core spins [33]. Then, several particle moments align in parallel with each other, promoted by the IPDI, leading to $D_m > D_{TEM}$ [34]. However, for the 30-nm particles, D_m is smaller than D_{TEM} over the whole temperature range because of its multi-domain structure, which arises from its particle size being far larger than the critical size of a single domain.

Figures 4 and 5 reveal that the loops recorded at 10 K for $CoFe_2O_4$ NPs and for the composites of $CoFe_2O_4$ and $CoFe_2$ contain jumps around H = 0. For the $CoFe_2O_4$ NPs, this phenomenon originates from

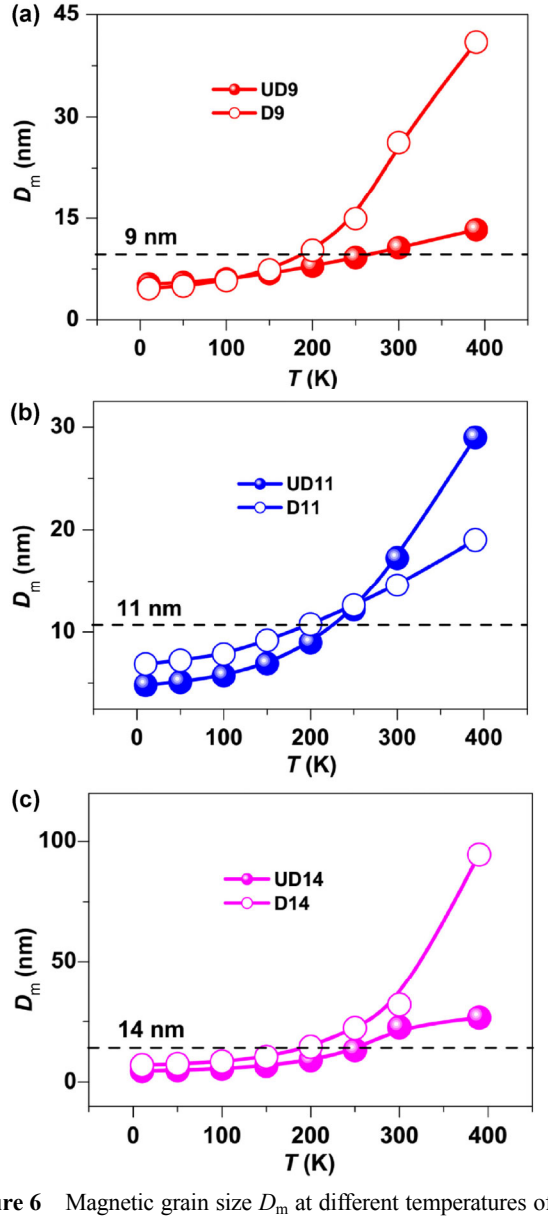

Figure 6 Magnetic grain size D_m at different temperatures of the unreduced, diluted and undiluted 9-nm (a), 11-nm (b), and 14-nm (c) NPs.

the reorientation of surface spins around particles [35]. However, in the case of the $CoFe_2O_4$/$CoFe_2$ composites, apart from the reorientation of surface spins, such jumps can also be attributed to the broad distribution of reversal fields of hard and soft species. Furthermore, these jumps also signify that no exchange coupling occurred between soft and hard species because in an exchange–coupled system, the magnetization could show an equivalent reversal behavior over the whole temperature region. With increasing temperature, the anisotropy field of all of the samples decreased

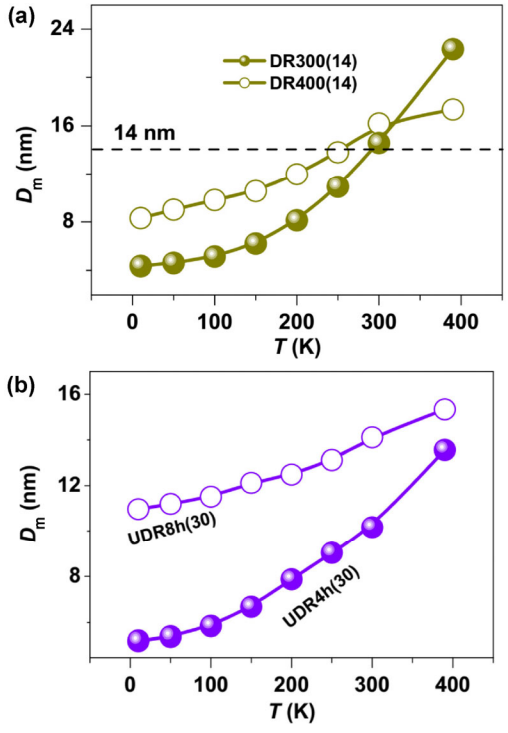

Figure 7 Magnetic grain size D_m of the reduced 14-nm (a) and 30-nm (b) NPs at different temperatures.

markedly, so the average reversal fields of the hard and soft phases may have been similar, resulting in the single-phase behavior of the loops.

Based on the obtained V_m values, the strength of the IPDI of all of the samples can be estimated by calculating H_{dip} according to Eq. (1), the $1/\lg H_{dip}$ values and the M_r/M_s ratios with added error bars (5%) are plotted against temperature (T) in Fig. 8 for the unreduced, diluted, and undiluted 9-, 11-, and 14-nm NPs and in Fig. 9 for the reduced 14- and 30-nm NPs.

As shown in Fig. 8, the M_r/M_s curves nearly overlap with the $1/\lg H_{dip}$ curves within a reasonable error range, even though the NPs were of different sizes and concentrations. However, as shown in Figs. 8(a), 8(d), 8(e), and 8(f), at low temperatures, the deviation between M_r/M_s and $1/\lg H_{dip}$ can be observed, and the slope of the M_r/M_s curve is smaller than that of the $1/\lg H_{dip}$ curve. This difference may have resulted from several competing effects, including surface effects, finite size effects, and interparticle interactions, as suggested by K. Maaz [29]. As shown in Fig. 6, the fact that $D_m < D_{TEM}$ confirms the existence of canted surface spins, and therefore, in the case of NPs with fixed size, it is reasonable to suggest that the deviation

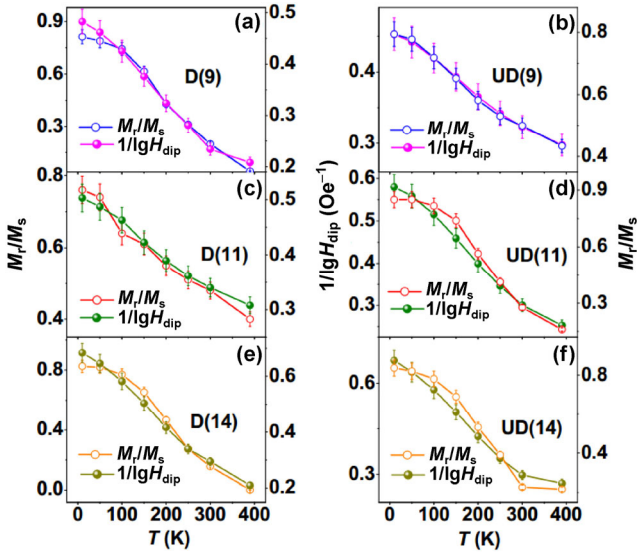

Figure 8 Plots of $1/\lg H_{dip}$ values and M_r/M_s ratios against temperature (T) for unreduced, diluted and undiluted 9-, 11- and 14-nm NPs, with error bars (5%) added.

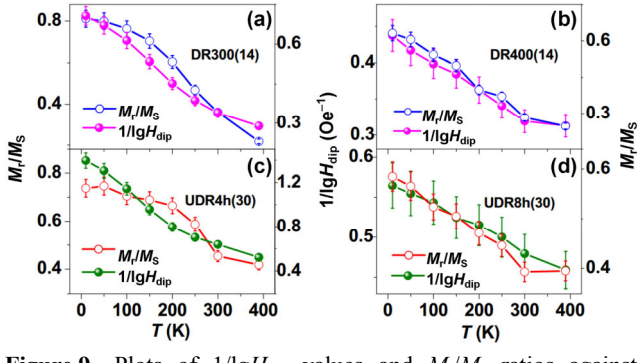

Figure 9 Plots of $1/\lg H_{dip}$ values and M_r/M_s ratios against temperature (T) for reduced 14- and 30-nm NPs, with error bars (5%) added.

between M_r/M_s and $1/\lg H_{dip}$ originated from the interactions between spins of the surface and the core and between surface spins of the neighboring particles.

In the case of the reduced 14- and 30-nm NPs containing $CoFe_2O_4$ and $CoFe_2$, as shown in Fig. 9, M_r/M_s deviated from $1/\lg H_{dip}$ for the slightly reduced DR300(14) and UDR4h(30), which can be attributed to several competing effects, as discussed below, whereas M_r/M_s matches well with $1/\lg H_{dip}$ for the heavily reduced DR400(14) and UDR8h(30). The interactions in $CoFe_2O_4/CoFe_2$ NPs occur at the interface (intraparticle) of $CoFe_2O_4$ and $CoFe_2$ and at the contacts between the NPs (interparticle). $CoFe_2O_4$ has a large magnetic anisotropy and can exert a

pinning action on the $CoFe_2$ phase, similar to the pinning effect of Fe oxide on Fe in Fe/Fe oxide NPs [33], which may be the reason for the deviation between M_r/M_s and $1/\lg H_{dip}$. This hypothesis is supported by the presence of an irreversible magnetization reversal field (H_{irr}) [25], which is defined as a magnetic field where the derivative (dM/dH) of the virgin curve has a peak. Figure 10 shows the field derivative dM/dH of the virgin curves for UDR4h(30) (a) and UDR8h(30) (b) samples at 10 K. Two peaks are located at H_{irr} = 3.4 and 20 kOe for UDR4h(30), and two are located at H_{irr} = 2.4 and 16 kOe for UDR8h(30). The lower field corresponds to the H_{irr} of $CoFe_2$ because pure $CoFe_2$ is a typical soft magnet, and its H_{irr} is approximately 0.9 kOe at 10 K, as shown in the inset of Fig. 10(a), whereas the higher field corresponds to the H_{irr} of hard $CoFe_2O_4$. UDR4h(30) contained more $CoFe_2O_4$ and less $CoFe_2$ than UDR8h(30), and $CoFe_2O_4$ exerted the pinning effect on the moment of $CoFe_2$, leading to the increased H_{irr} of $CoFe_2$. The UDR8h(30) sample contained more $CoFe_2$; therefore, the moment of $CoFe_2$ could not be fully pinned by $CoFe_2O_4$, leading to the lower H_{irr} of $CoFe_2$ in the UDR8h(30) sample. It is possible that the greater amount of $CoFe_2$ in UDR8h(30) polarized the moments of $CoFe_2O_4$, resulting in the smaller H_{irr} of $CoFe_2O_4$ than that of UDR4h(30) [33].

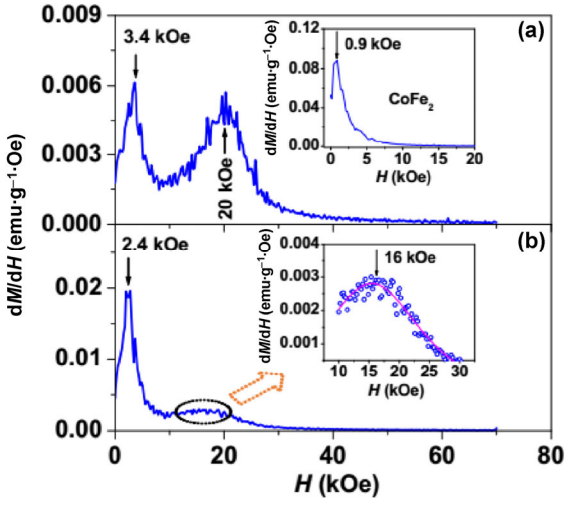

Figure 10 Field derivative (dM/dH) of the virgin curves for UDR4h(30) (a) and UDR8h(30) (b) at 10 K. The inset in (a) shows the dM/dH curve for pure $CoFe_2$. The inset in (b) shows the local dM/dH data (empty circles) around 16 kOe of the UDR8h(30) sample with the curve of Lorentz fit (solid line) in order to find the peak position.

These interactions in the $CoFe_2O_4/CoFe_2$ NPs affected the moment reversal and consequently affected the M_r/M_s ratio.

However, compared with DR300(14) and UDR4h(30), the heavily reduced DR400(14) and UDR8h(30) samples had greater $CoFe_2$ contents because they were reduced in H_2 at a higher temperature or for a longer time. Therefore, DR400(14) and UDR8h(30) had larger particle moments and hence stronger interparticle dipolar interactions, which overcame other effects such as surface spin and interactions between $CoFe_2O_4$ and $CoFe_2$, consequently making the correlation between M_r/M_s and $1/\lg H_{dip}$ obey $M_r/M_s \propto 1/\lg H_{dip}$.

4 Conclusions

Well-dispersed, uniform $CoFe_2O_4$ NPs with sizes of 9, 11, 14, and 30 nm were synthesized. Some of the 9-, 11-, and 14-nm NPs were diluted in a SiO_2 matrix to change their interparticle distance, and some diluted 14-nm and undiluted 30-nm NPs were reduced by H_2 under different conditions to change the moment and the anisotropy of the NPs. These samples were used as model systems to reveal the intrinsic correlation between M_r/M_s and IPDI, the strength of which was estimated by H_{dip}.

For the diluted and undiluted 9-, 11-, and 14-nm NPs that were not reduced, the correlation between M_r/M_s and H_{dip} followed $M_r/M_s \propto 1/\lg H_{dip}$ regardless of the particle size and interparticle distance. Slight deviation from $M_r/M_s \propto 1/\lg H_{dip}$, occurring at low temperatures, can be attributed to the effects of surface spin. In the case of the reduced, diluted 14-nm and undiluted 30-nm NPs, the relationship between M_r/M_s and H_{dip} deviated from $M_r/M_s \propto 1/\lg H_{dip}$ for the slightly reduced NPs because of the pinning effect of $CoFe_2O_4$ on $CoFe_2$. However, the heavily reduced NPs followed $M_r/M_s \propto 1/\lg H_{dip}$ because the strong interparticle dipolar interaction is a dominant factor affecting M_r/M_s.

Acknowledgements

This work was supported by the National Natural Science Foundation of China (Nos. 51471001, 11174004, and 11304001).

References

[1] Zhao, X. F.; Xu, S. L.; Wang, L. Y.; Duan, X.; Zhang, F. Z. Exchange-biased $NiFe_2O_4$/NiO nanocomposites derived from NiFe-layered double hydroxides as a single precursor. *Nano Res.* **2010**, *3*, 200–210.

[2] Wang, X.; Zhuang, J.; Peng, Q.; Li, Y. D. A general strategy for nanocrystal synthesis. *Nature* **2005**, *437*, 121–124.

[3] Yavuz, C. T.; Mayo, J. T.; Yu, W. W.; Prakash, A.; Falkner, J. C.; Yean, S.; Cong, L. L.; Shipley, H. J.; Kan, A.; Tomson, M. et al. Low-field magnetic separation of monodisperse Fe_3O_4 nanocrystals. *Science* **2006**, *314*, 964–967.

[4] Triet, N. M.; Trung, T. Q.; Hien, N. T. D.; Siddiqui, S.; Kim, D.-I.; Lee, J. C.; Lee, N.-E. A flexible magnetoelectric field-effect transistor with magnetically responsive nanohybrid gate dielectric layer. *Nano Res.* **2015**, *8*, 3421–3429.

[5] Li, S. L.; Li, A. H.; Zhang, R. R.; He, Y. Y.; Zhai, Y. J.; Xu, L. Q. Hierarchical porous metal ferrite ball-in-ball hollow spheres: General synthesis, formation mechanism, and high performance as anode materials for Li-ion batteries. *Nano Res.* **2014**, *7*, 1116–1127.

[6] Ooi, F.; DuChene, J. S.; Qiu, J. J.; Graham, J. O.; Engelhard, M. H.; Cao, G. X.; Gai, Z.; Wei, W. D. A facile solvothermal synthesis of octahedral Fe_3O_4 nanoparticles. *Small* **2015**, *11*, 2649–2653.

[7] Liu, Y. X.; Wang, D. S.; Shi, J. X.; Peng, Q.; Li, Y. D. Magnetic tuning of upconversion luminescence in lanthanide-doped bifunctional nanocrystals. *Angew. Chem., Int. Ed.* **2013**, *52*, 4366–4369.

[8] Metin, Ö.; Özkar, S.; Sun, S. H. Monodisperse nickel nanoparticles supported on SiO_2 as an effective catalyst for the hydrolysis of ammonia–borane. *Nano Res.* **2010**, *3*, 676–684.

[9] Min, H.; Jo, S. M.; Kim, H. S. Efficient capture and simple quantification of circulating tumor cells using quantum dots and magnetic beads. *Small* **2015**, *11*, 2536–2542.

[10] Mendelev, V. S.; Ivanov, A. O. Ferrofluid aggregation in chains under the influence of a magnetic field. *Phys. Rev. E* **2004**, *70*, 051502.

[11] Huber, D. L. Synthesis, properties, and applications of iron nanoparticles. *Small* **2005**, *1*, 482–501.

[12] Laureti, S.; Varvaro, G.; Testa, A. M.; Fiorani, D.; Agostinelli, E.; Piccaluga, G.; Musinu, A.; Ardu, A.; Peddis, D. Magnetic interactions in silica coated nanoporous assemblies of $CoFe_2O_4$ nanoparticles with cubic magnetic anisotropy. *Nanotechnology* **2010**, *21*, 315701.

[13] Prado, Y.; Mazerat, S.; Rivière, E.; Rogez, G.; Gloter, A.; Stéphan, O.; Catala, L.; Mallah, T. Magnetization reversal in $CsNi^{II}Cr^{III}(CN)_6$ coordination nanoparticles: Unravelling surface anisotropy and dipolar interaction effects. *Adv. Funct. Mater.* **2014**, *24*, 5402–5411.

[14] Ewerlin, M.; Demirbas, D.; Brüssing, F.; Petracic, O.; Ünal, A. A.; Valencia, S.; Kronast, F.; Zabel, H. Magnetic dipole and higher pole interaction on a square lattice. *Phys. Rev. Lett.* **2013**, *110*, 177209.

[15] Woińska, M.; Szczytko, J.; Majhofer, A.; Gosk, J.; Dziatkowski, K.; Twardowski, A. Magnetic interactions in an ensemble of cubic nanoparticles: A Monte Carlo study. *Phys. Rev. B* **2013**, *88*, 144421.

[16] Stoner, E. C.; Wohlfarth, E. P. A mechanism of magnetic hysteresis in heterogeneous alloys. *Phil. Trans. R. Soc. Lond. A* **1948**, *240*, 599–642.

[17] Vargas, J. M.; Nunes, W. C.; Socolovsky, L. M.; Knobel, M.; Zanchet, D. Effect of dipolar interaction observed in iron-based nanoparticles. *Phys. Rev. B* **2005**, *72*, 184428.

[18] Zan, F. L.; Ma, Y. Q.; Ma, Q.; Zheng, G. H.; Dai, Z. X.; Wu, M. Z.; Li, G.; Sun, Z. Q.; Chen, X. S. One-step hydrothermal synthesis and characterization of high magnetization $CoFe_2O_4$/$Co_{0.7}Fe_{0.3}$ nanocomposite permanent magnets. *J. Alloys Compd.* **2013**, *553*, 79–85.

[19] Kurtan, U.; Topkaya, R.; Baykal, A. Sol–gel auto-combustion synthesis of PVP/$CoFe_2O_4$ nanocomposite and its magnetic characterization. *Mater. Res. Bull.* **2013**, *48*, 4889–4895.

[20] Mumtaz, A.; Maaz, K.; Janjua, B.; Hasanain, S. K.; Bertino, M. F. Exchange bias and vertical shift in $CoFe_2O_4$ nanoparticles. *J. Magn. Magn. Mater.* **2007**, *313*, 266–272.

[21] Cannas, C.; Musinu, A.; Peddis, D.; Piccaluga, G. Synthesis and characterization of $CoFe_2O_4$ nanoparticles dispersed in a silica matrix by a sol–gel autocombustion method. *Chem. Mater.* **2006**, *18*, 3835–3842.

[22] Diodati, S.; Pandolfo, L.; Caneschi, A.; Gialanella, S.; Gross, S. Green and low temperature synthesis of nanocrystalline transition metal ferrites by simple wet chemistry routes. *Nano Res.* **2014**, *7*, 1027–1042.

[23] Leite, G. C. P.; Chagas, E. F.; Pereira, R.; Prado, R. J.; Terezo, A. J.; Alzamora, M.; Baggio-Saitovitch, E. Exchange coupling behavior in bimagnetic $CoFe_2O_4$/$CoFe_2$ nano-composite. *J. Magn. Magn. Mater.* **2012**, *324*, 2711–2716.

[24] Li, Y. F.; Hu, Y. J.; Huo, J. C.; Jiang, H.; Li, C. Z.; Huang, G. J. Stable core shell Co_3Fe_7–$CoFe_2O_4$ nanoparticles synthesized via flame spray pyrolysis approach. *Ind. Eng. Chem. Res.* **2012**, *51*, 11157–11162.

[25] Soares, J. M.; Cabral, F. A. O.; de Araújo, J. H.; Machado, F. L. A. Exchange-spring behavior in nanopowders of $CoFe_2O_4$–$CoFe_2$. *Appl. Phys. Lett.* **2011**, *98*, 072502.

[26] Li, W. M.; Wong, S. K.; Herng, T. S.; Yap, L. K.; Sim, C. H.; Yang, Z. C.; Chen, Y. J.; Shi, J. Z.; Han, G. C.; Xue, J. M. et al. Perpendicular magnetic clusters with configurable

domain structures via dipole–dipole interactions. *Nano Res.* **2015**, *8*, 3639–3650.

[27] Wang, C.; Peng, S.; Lacroix, L.-M.; Sun, S. H. Synthesis of high magnetic moment CoFe nanoparticles via interfacial diffusion in core/shell structured Co/Fe nanoparticles. *Nano Res*. **2009**, *2*, 380–385.

[28] Skomski, R.; Coey, J. M. D. Giant energy product in nanostructured two-phase magnets. *Phys. Rev. B* **1993**, *48*, 15812–15816.

[29] Mazz, K.; Usman, M.; Karim, S.; Mumtaz, A.; Hasanain, S. K.; Bertino, M. F. J. Magnetic response of core-shell cobalt ferrite nanoparticles at low temperature. *J. Appl. Phys.* **2009**, *105*, 113917.

[30] Kneller, E. F.; Hawig, R. The exchange-spring magnet: A new material principle for permanent magnets. *IEEE Trans. Magn.* **1991**, *27*, 3588–3560.

[31] Hyeon, T.; Chung, Y.; Park, J.; Lee, S. S.; Kim, Y. W.; Park, B. H. Synthesis of highly crystalline and monodisperse cobalt ferrite nanocrystals. *J. Phys. Chem. B* **2002**, *106*, 6831−6833.

[32] Lakshmi, N.; Bhargava, H.; Suwalka, O. P.; Venugopalan, K.; Sebastian, V., Reddy, V. R.; Gupta, A. Magnetic properties resulting from core-shell interactions in nanosized $Ni_{0.25}Co_{0.25}Zn_{0.5}Fe_2O_4$. *Phys. Rev. B* **2009**, *80*, 174425.

[33] Del Bianco, L.; Fiorani, D.; Testa, A. M.; Bonetti, E.; Savini, L.; Signoretti, S. Magnetothermal behavior of a nanoscale Fe/Fe oxide granular system. *Phys. Rev. B* **2002**, *66*, 174418.

[34] Fu, J. C.; Zhang, J. L.; Peng, Y.; Zhao, J. G.; Tan, G. G.; Mellors, N. J.; Xie, E. Q.; Han, W. H. Unique magnetic properties and magnetization reversal process of $CoFe_2O_4$ nanotubes fabricated by electrospinning. *Nanoscale* **2012**, *4*, 3932–3936.

[35] Quesada, A.; Rubio-Marcos, F.; Marco, J. F.; Mompean, F. J.; García-Hernández, M.; Fernández, J. F. On the origin of remanence enhancement in exchange-uncoupled $CoFe_2O_4$-based composites. *Appl. Phys. Lett.* **2014**, *105*, 202405.